Effect of Flux Addition on the Microstructure and Hardness of TiC-Reinforced Ferrous Surface Composite Layers Fabricated by High-Energy Electron Beam Irradiation

SEONG-HUN CHOO, SUNGHAK LEE, and SOON-JU KWON

Surface composites reinforced with TiC particulates were fabricated by high-energy electron-beam irradiation. In order to investigate the effects of flux addition on the TiC dispersion in surface composite layers, four kinds of powder mixtures were made by mixing TiC with 5, 10, 20, and 40 wt pct of the flux components (MgO-CaO). To fabricate TiC-reinforced surface composites, the TiC-flux mixtures were deposited evenly on a plain carbon steel substrate, which was subjected to electron-beam irradiation. Microstructural analysis was conducted using X-ray diffraction and Mossbauer spectroscopy as well as optical and scanning electron microscopy. The microstructure of the surface composites was composed of a melted region, an interfacial region, a coarse-grained heat-affected zone (HAZ), a fine-grained HAZ, and an unaltered original substrate region. TiC agglomerates and residual pores were found in the melted region of materials processed without flux, but the number of agglomerates and pores was significantly decreased in materials processed with a considerable amount of flux. As a result of irradiation, TiC particles were homogeneously distributed throughout the melted region of 2.5 mm in thickness, whose hardness was greatly increased. The optimum flux amount, which resulted in surface composites containing homogeneously dispersed TiC particles, was found to be in the range of 10 to 20 pct to obtain excellent surface composites.

I. INTRODUCTION

GENERALLY , metal-matrix composites reinforced with ceramics have excellent properties compared to unreinforced metals because they show high strength, high elastic modulus, and improved resistance to wear and oxidation. In particular, because TiC-reinforced ferrous or nickel-base composites are very hard and have thermodynamically stable TiC particles inside the matrix, whose structure can be modified by subsequent heat treatment,[1,2] they can be applied to structures requiring resistance to abrasion and corrosion and high-temperature properties. Ferrous composites reinforced with titanium carbides are typically fabricated by a powder-metallurgy route through the process of mixing TiC powders with steel powders, densification, and sintering and are commercialized in such brand names as Ferrotic, TiCAlloy, and Ferrotitanit.[3,4,5] In this fabrication method, homogeneous mixing of TiC and steel powders is hard to achieve, and the surface of both powders is prone to contamination during mixing. Another way to fabricate TiC-reinforced composites is by casting using liquid Fe-Ti-C alloys,[6,7] Fe-Ti and Fe-C alloys,[8,9] or Fe-Ti alloys and graphite[10] to obtain thermally stable carbides from the liquid by *in situ* precipitation of TiC particles. However, this method demands a complex process to achieve a uniform TiC particle dispersion. Other fabrication techniques such as liquid-phase sintering,[11] self-sustaining high-temperature synthesis,[12] plasma spraying,[13] and surface alloying using a laser[14–18] have also been used. Recently, new attempts have been made by direct irradiation using a high-energy electron beam in order to achieve surface hardening or surface alloying.[19,20]

When a material surface is irradiated by a high-energy electron beam of several MeV, electron energy is transferred to the material surface by collisions with the electrons of the material. The energy from these electrons is transferred nearly instantaneously to the lattice as heat[21] that is high enough to melt materials having high melting temperatures. Upon irradiation of a metal surface on which ceramic powders are evenly deposited, the metal surface is melted, while the ceramic powders are either partially or completely melted and then precipitated again during solidification, thereby fabricating a surface composite. This electron-beam-irradiation method rarely forms pores or cracks because of high thermal efficiency and homogeneous heating and cooling. It can be continuously performed due to its application in air, and thus can treat a very large area conveniently at one time, which makes it advantageous for the fabrication of large-sized structures or parts and for mass production. Advantages of this irradiation method are (1) a discontinuity in chemical and mechanical properties between the melted region and the substrate does not exist, in distinction from other surface treatments such as spraying and evaporation; (2) slag formation is minimized; (3) ceramic powders can be saved by alloying only the surface region; (4) productivity is high, *e.g.*, 72 m^2 area per hour; and (5) the fabrication cost is reduced because energy of 0.6 to 0.8 kWh is required to treat 1 kg of powder.

In the present study, a simple process is suggested to fabricate TiC-reinforced ferrous composites with improved surface properties by evenly depositing TiC powders on the surface of a plain carbon-steel substrate and irradiating it with a high-energy electron beam. It is important to optimize process conditions in order to control the final microstructures of the surface composite layers during solidification.

SEONG-HUN CHOO, Postdoctoral Research Associate, and SUNGHAK LEE, Professor, Center for Advanced Aerospace Materials, and SOON-JU KWON, Professor, Department of Materials Science and Engineering, are with Pohang University of Science and Technology, Pohang, 790-784 Korea.

Manuscript submitted January 21, 1999.

A mixture of MgO and CaO powders was used as flux to obtain a uniform TiC particle dispersion, and four kinds of specimens were fabricated by varying the mixing ratios of TiC and flux in order to compare the resulting various microstructures, chemical compositions, and hardnesses.

II. EXPERIMENTAL

Ceramic reinforcements used in this study are TiC powders fabricated by Atlantic Equipment Engineers Co., Ltd. (Bergenfield, NJ), with a 99 pct purity and a size of 2 to 5 μm. Stoichiometric TiC is a stable and hard compound having the NaCl-type fcc structure, a density of 4.94 g/cm^3, and a melting temperature of 3160 °C.[22] A plain carbon-steel plate (40 × 50 × 20 mm) was used as a substrate. The steel's compositions are Fe-0.10C-0.24Si-0.56Mn-0.16Cu-0.08Ni-0.06Cr-0.02Al-0.01P-0.03S (all in wt pct). In the present study, MgO and CaO powders were selected as flux components and mixed with a 1:1 ratio (in wt pct) for convenience. It has been reported that the role of MgO is to control the molten fluidity and that of CaO is to reduce the impurities during welding or brazing.[23,24] After mixing TiC powders with the MgO and CaO components, the mixture was dried at 200 °C for 30 minutes. In order to survey the effects of flux addition on TiC dispersion in surface composite layers, four kinds of TiC-flux mixtures were made by mixing TiC with 5, 10, 20, and 40 wt pct of the flux components. For convenience, these mixtures are referred to as "T5," "T10," "T20," and "T40," respectively. The surface of the steel substrates was ground and cleaned, and the TiC-flux mixtures were deposited on it homogeneously to about 1-mm thickness. The mixtures were pressed at 300 kPa and then irradiated with a high-energy electron beam. Figure 1 is a schematic diagram showing the fabrication procedures.

A high-voltage electron accelerator at the Budker Institute of Nuclear Physics (Novosibirsk, Russia) was used for irradiation. This accelerator has energy ranges of 1.0 to 2.5 MeV and a maximum power of 80 kW. Irradiation conditions depend on process parameters such as beam power, beam current, and beam traveling speed. The process parameters used in this study are listed in Table I. The flux components, MgO and CaO, form slag crusts after irradiation, and thus, no flux components exist in the surface composite layers.

Table I. Irradiation Conditions of High-Energy Electron Beam for the TiC-Reinforced Ferrous Surface Composites

Electron energy	1.4 MeV
Beam current	28 mA
Beam traveling speed	1 cm/s
Beam diameter	1.2 cm
Scanning width	4 cm
Scanning frequency	20 Hz
Distance from diaphragm to specimen	9 cm

After sectioning the irradiated specimen parallel to the irradiation direction, the microstructure was examined using optical microscopy and scanning electron microscopy (SEM). Phases in the surface composite specimens were analyzed by X-ray diffraction and Mossbauer spectroscopy, and volume fractions of TiC particles were measured using an image analyzer.

A 20 mCi Co^{57} gamma-ray source in Rh matrix was used for the Mossbauer spectroscopic study. Thin disk-type specimens (about 50 μm in thickness and 10 mm in diameter) were prepared from the surface composite layers. The transmission-mode resonance absorption spectrum was taken. The spectrum was least-squares fitted with the subspectra relevant to iron carbides and iron phases of bct-Fe, of bcc-Fe, and of fcc-Fe.[25,26] Microhardness was measured along the depth from the irradiated surface using a Vickers hardness tester under a 500-g load.

III. RESULTS

A. *Microstructure of Surface Composite Layers*

Figures 2(a) through (d) are low-magnification optical micrographs showing the overall microstructures of the four TiC-reinforced ferrous surface-composite specimens. The surface of the carbon steel substrate as well as powder mixtures is melted, and the melted region is composed of partially or completely melted and reprecipitated TiC particles in matrix phase. The thickness of the surface composite specimens shows minor variations but is approximately 2.5 mm in all the specimens. The interface between the melted

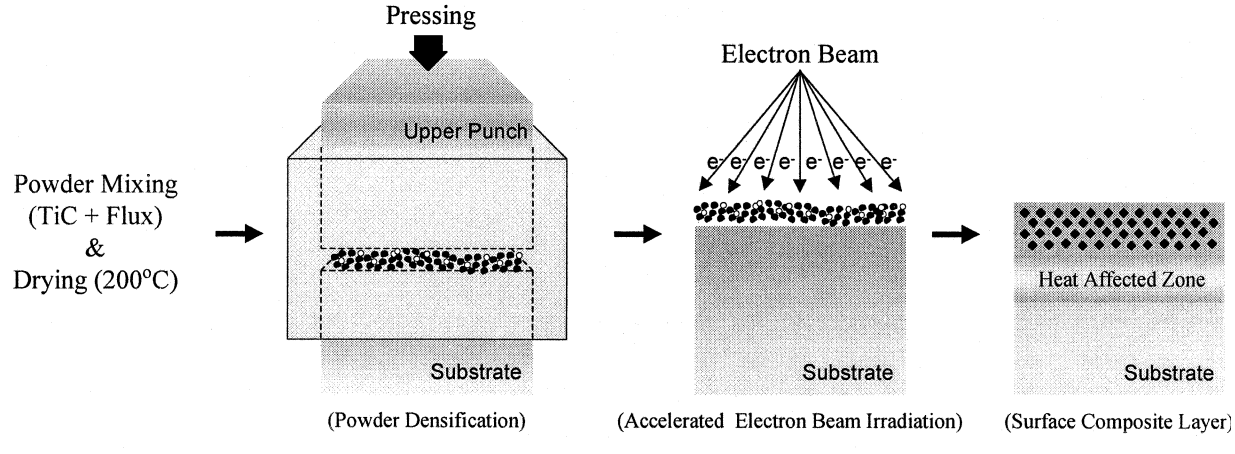

Fig. 1—Schematic diagram showing the fabrication procedures for the TiC-reinforced surface composite specimens.

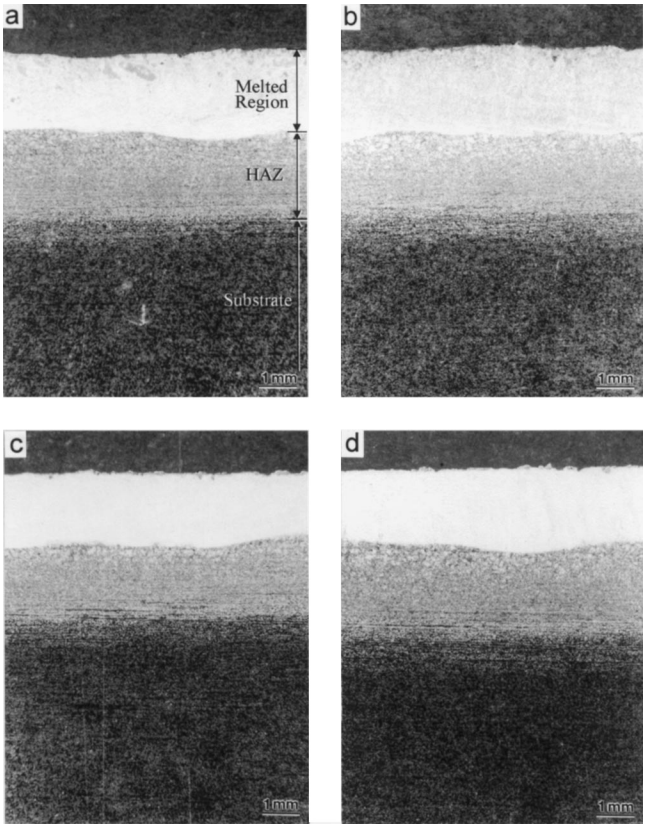

Fig. 2—Low-magnification optical micrographs of the TiC-reinforced surface composite specimens irradiated with a high-energy electron beam: (*a*) T5, (*b*) T10, (*c*) T20, and (*d*) T40 specimens. The TiC powders and the surface of the steel substrate were melted by irradiation, and the interface between the melted region and the HAZ is clearly visible. Nital etched.

and the unmelted regions is clearly visible. Below the melted region lies a heat-affected zone (HAZ) of about 2.5 mm in thickness.

Figures 3(a) through (e) are optical micrographs of the composite specimens. In the upper part of the melted region of the T5 specimen, coarse TiC agglomerates and pores are observed, as indicated by arrows in Figure 3(a). Figure 3(b) is a higher magnification micrograph of the area marked by "A" in Figure 3(a). These TiC agglomerates look similar to those formed in a sintered reaction, and are concentrated in the upper melted region because of the density difference between the TiC and the steel substrate. In the T10 specimen, TiC agglomerates are also observed, together with micropores inside the agglomerates, but a fraction of agglomerates and pores is considerably reduced in comparison to the T5 specimen (Figure 3(c)). The TiC agglomerates continue to decrease in number as the flux addition increases and, thus, almost completely disappear in the T20 and T40 specimens (Figures 3(d) and (e)).

Figures 4(a) through (f) are SEM micrographs showing the TiC particles in the melted region. The T5 specimen is mainly composed of radially grown dendrites of primary TiC particles, together with faceted rosette-shaped and fine cuboidal TiC particles (Figure 4(a)). The T10 specimen also shows the same solidification behavior as in the T5 specimen, except that the TiC particle size is slightly reduced (Figure 4(b)). Figure 4(c) is a higher magnification SEM micrograph of the T10 specimen and shows faceted rosette-shaped primary TiC particles and fine needle-shaped formed between primary TiC particles by a ternary eutectic reaction (marked by an arrow). In the T20 specimen, only cuboidal TiC particles of about 3 to 4 μm in size are evenly distributed in the melted region (Figure 4(d)). The TiC volume fraction is radically reduced in the T40 specimen because only cuboidal TiC particles of about 1 μm in size are found (Figure 4(e)). It is interesting to note that a few eutectic TiC particles are precipitated along solidification-cell boundaries in the T40 specimen (Figure 4(f)). When the matrix of the melted region is observed in the nital-etched condition, the T40 specimen is mainly composed of bainite together with a small amount of ferrite (Figure 5). The matrices of the other specimens are also composed of mostly bainite, as in the T40 specimen.

The volume fraction and average size of the TiC particles precipitated in the melted region are listed in Table II. The volume fraction of TiC agglomerates in the T5 specimen is about 30 pct, and the total TiC volume fraction reaches about 50 pct if primary and fine eutectic TiC particles are counted. The agglomerate volume fraction decreases to about 8 pct in the T10 specimen, and the total TiC fraction is about 28 pct. In the T20 and T40 specimens, the total TiC fraction is reduced to 13 and 2 pct, respectively, and TiC agglomerates are not found.

B. *Microstructure of HAZ*

Figures 6(a) through (f) are optical micrographs of the T20 specimen, showing the microstructural modification from the interfacial region to the unaltered substrate region. A distinct interface between the melted region and the HAZ exists, as shown in Figure 6(a). Below the interface are a coarse-grained HAZ, a fine-grained HAZ, and an unaltered region. Such a sequence of microstructures is similar to the case of a welded-steel HAZ.[27,28] The HAZ adjacent to the interfacial region consists of a coarse-grained structure of ferrite and bainite (Figure 6(b)). The ferrite here is characterized by a peculiar growth pattern, which occurs radially in one direction, unlike the equiaxed or elongated shape observed in an ordinary ferrite-pearlite structure. This happens under an extremely low cooling rate when ferrite grows in a Widmanstatten pattern from the prior austenite grain boundary into the interior of the austenite grain.[29] Below the coarse-grained HAZ exists the fine-grained HAZ, which is mainly composed of ferrite (Figure 6(c)). Figures 6(d) and (e) show a decomposition process of pearlite in the region below the fine-grained HAZ, because this region was heated up to ($\alpha + \gamma$) region during irradiation. Figure 6(f) is a micrograph of the unaltered region, which consists of ferrite and pearlite.

C. *Phase Analysis of Surface Composite Layers*

Figures 7(a) through (d) are the X-ray diffraction patterns of surface composite layers, confirming the presence of TiC particles and ferrite. The TiC intensity decreases with increasing flux-mixing ratio. A small amount of retained austenite is also present in the T5, T10, and T20 specimens, because the carbon content of the matrix might be increased by the melting of TiC powders.

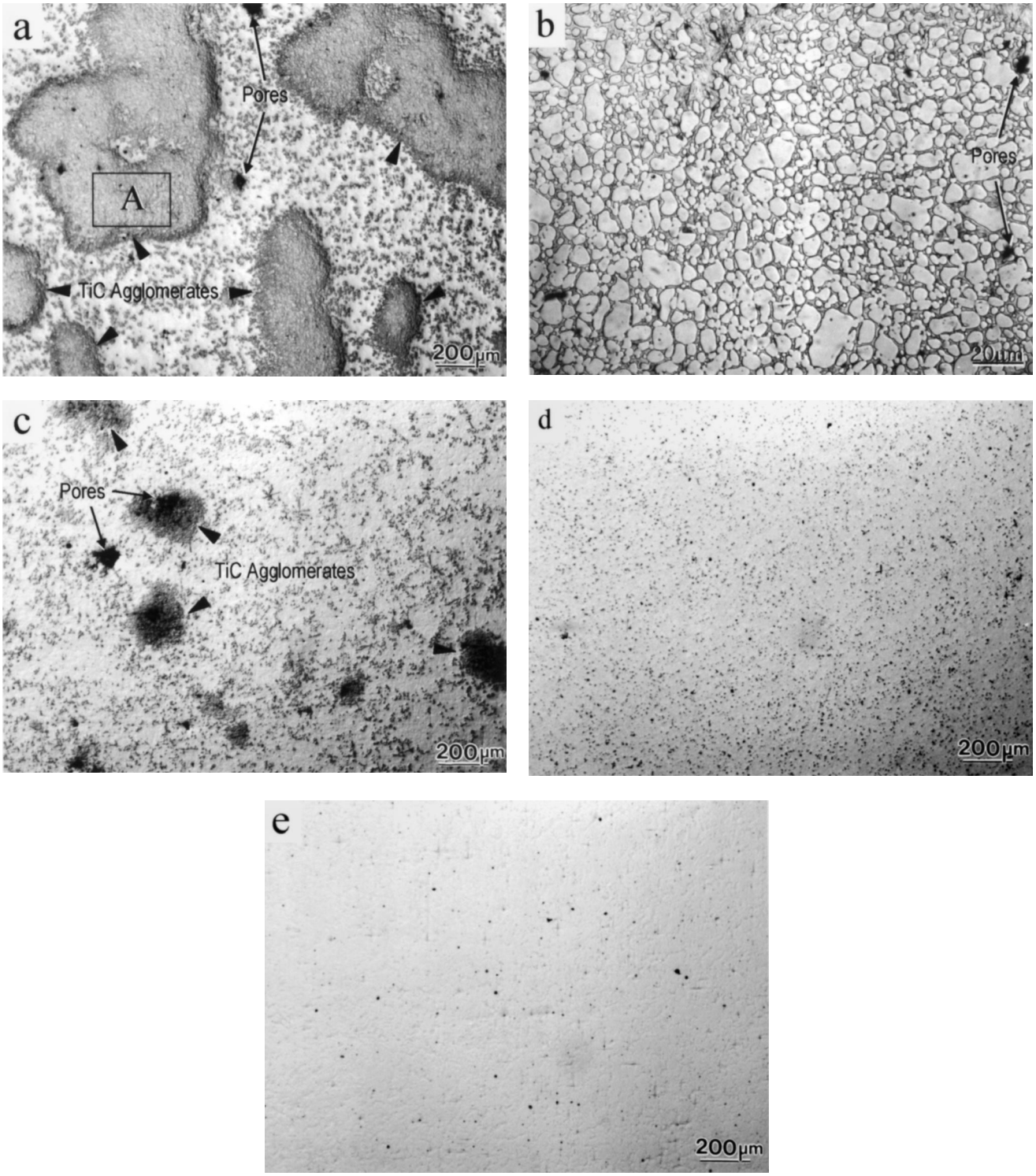

Fig. 3—Optical micrographs of the melted region of (*a*) and (*b*) the T5, (*c*) the T10, (*d*) the T20, and (*e*) the T40 specimens. (b) is a higher magnification micrograph of the area marked "A" in (a). Arrows indicate TiC agglomerates and pores in (a) through (c). Not etched.

Mossbauer spectroscopy is advantageous for its capability to provide qualitative and quantitative information on the fraction of iron-containing phases in steels, which is hard to obtain from other analysis methods such as X-ray analysis. Thus, when used complementarily with other analyses, it can produce very important insights. The present study employs Mossbauer spectroscopy to identify the phases present in the irradiated surface composite layers and to quantitatively measure their fractions. It should be noted that the Mossbauer analysis does not give information on compounds of noniron alloying elements such as TiC, since only the signal from the iron can be detected in this experiment.

Table III lists the reported hyperfine parameters, with which the least-squares fitting of the Mossbauer spectra can

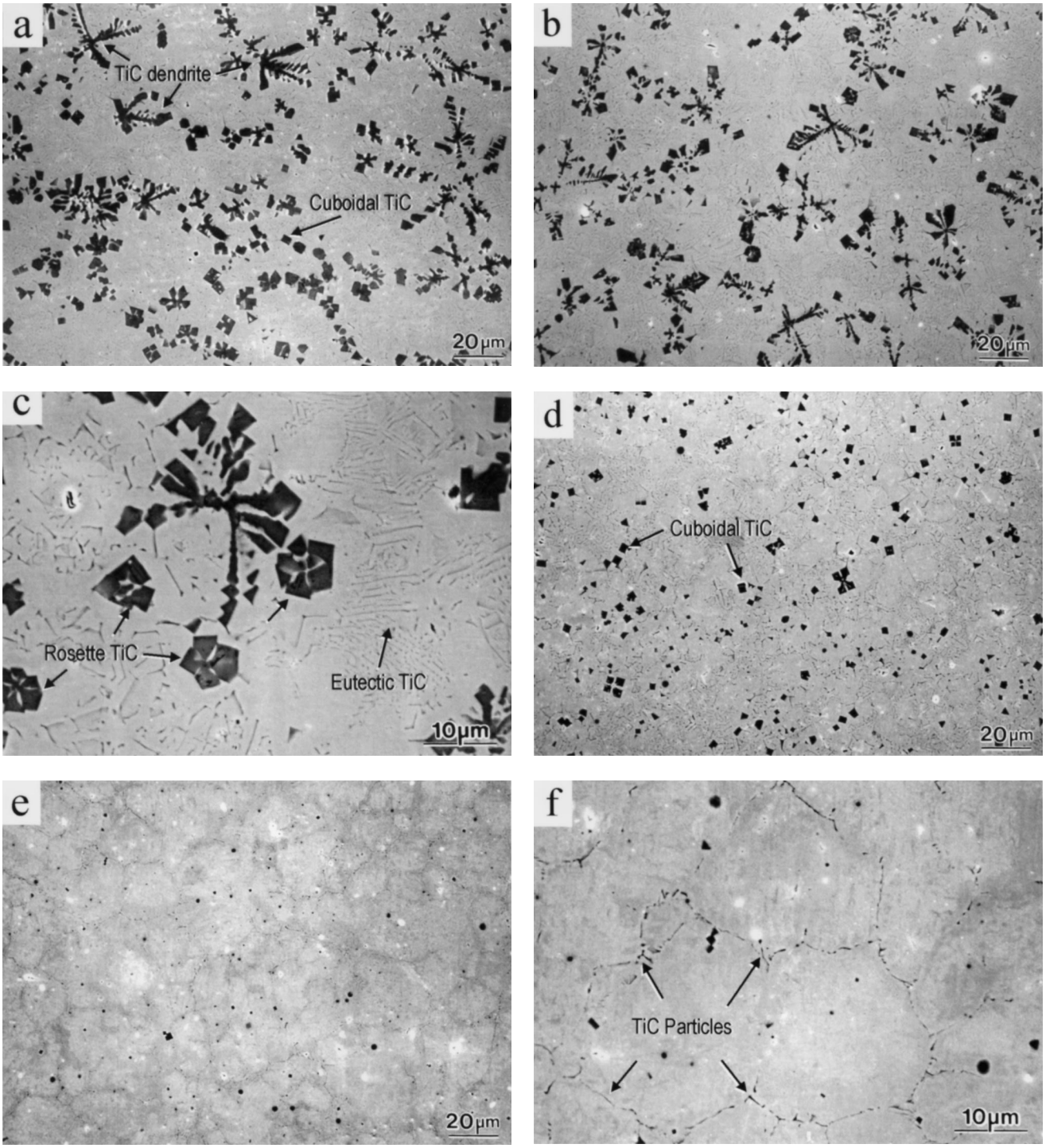

Fig. 4—SEM micrographs of the melted region of (*a*) the T5, (*b*) and (*c*) the T10, (*d*) the T20, and (*e*) and (*f*) the T40 specimens. Arrows indicate TiC dendrites, faceted rosette-shaped TiC particles, cuboidal TiC particles, and needle-shaped eutectic TiC particles precipitated along solidification cell boundaries. Not etched.

be conducted. Pure ferrite has a single sextet (bcc-Fe), whose hyperfine field is about 33 Tesla. The bct phase (martensite), however, includes significant amounts of carbon at the interstitial sites. Thus, the spectrum consists of at least three sextets, depending on the location of carbon atoms at the first, the second nearest interstitial sites, and further (bct-Fe(1), bct-Fe(2), and bct-Fe).[30] Substitutional elements, such as manganese and silicon, are soluble in both bcc and bct structures and strongly disturb the local environment of iron atoms to produce several subspectra. Due to the strong disturbance, there seems to be no resolution to differentiate the patterns of bct-Fe and bcc-Fe, where substitutional elements are incorporated. The only choice is to designate the spectra simply as Fe-M(1) and Fe-M(2) for those Fe's with an alloying element at the first and the second nearest substitutional sites, respectively. (When the element locates further apart, the spectrum becomes bcc-Fe or bct-Fe.) The nonmagnetic fcc phase (austenite) has a highly isotropic structure

Fig. 5—Optical micrograph of the melted region of the T40 specimen, showing the matrix microstructure composed of bainite, together with a small amount of ferrite. Nital etched.

Table II. Quantitative Analysis Results of the Surface Composite Specimens Fabricated by a High-Energy Electron Beam

Specimen	Volume Fraction of TiC Particles (Pct)				Average Size (μm)
	TiC Agglomerate	Primary TiC	Eutectic TiC	Total TiC	
T5	29.6	15.8	5.2	50.6	—
T10	7.9	13.3	6.5	27.7	—
T20	0	4.7	8.7	13.4	3.5
T40	0	0.5	1.2	1.7	1.12

and produces a singlet.[31] Fe_3C carbide has two equivalent sites in the crystal structure and, thus, produces two magnetic sextets. The hyperfine magnetic fields are 20.5 and 19.7 Tesla for Fe_3C(a) and Fe_3C(b), respectively.[32–35] In a rapidly cooled sample, some cementites should be very fine. This requires an extra spectrum for super paramagnetic cementite, Fe_3C(s), to analyze the sample where martensite and/or bainite are the constituents.[36] The sextet of Fe_5C_2,[35] another magnetic carbide, is distinct due to the hyperfine magnetic field of 23 Tesla.

The integral intensity of each subspectrum (the area below the base line) provides an estimation of iron population in each phase. The volume fractions of steel phases have hardly been mentioned in the Mossbauer spectrum analysis, because the gamma ray recoil-free fractions are not exactly known for the phases. At a constant experimental temperature, however, the recoil-free fraction is solely determined by the Debye temperature of the phase.[37] The Debye temperatures are about 470 K for bcc-Fe[38] and 480 K for Fe_3C.[32] The value for the bct-Fe is not available at this time, but should be between 470 K (bcc-Fe) and 480 K (Fe_3C), as is the mechanical rigidity of the bct-Fe. Such a negligible difference in the Debye temperatures imply that the fraction of a subspectrum represents well the atomic population of iron in each phase without a serious correction for the recoil-free fraction. Furthermore, the atomic fraction and the volume fraction differ less than 10 pct (relative), since the volume per iron atom is about 12 A^3 in iron phases (bcc, bct, and fcc) and is about 13 A^3 in carbides. (The volume per iron atom was obtained by dividing the volume of a unit cell with the number of iron atoms in the cell.) In these regards, the area fraction of the subspectrum is a good estimation of the fraction of the corresponding phase. It should be noted that the bcc phase could be the constituent of pure ferrite, pearlite, and bainite. Thus, the relevant structure must be assigned with the help of the microstructural observations.

Figures 8(a) through (d) are Mossbauer spectra of the near-surface melted region and show peak positions of subspectra. The bct-Fe was not detected in any specimens. Correlating these results with the microstructure of Figure 5, the bcc phase in these surface composites can be assigned to be bainite (or ferrite), since pearlite cannot be identified from the microstructure. The fraction of each phase was determined according to the aforementioned method and is listed in Table IV. The surface composite layers are composed of 89 to 96 pct bainite (or ferrite), 2 to 3 pct cementite, and 2 to 8 pct austenite, depending on the flux-mixing ratio.

D. *Hardness*

The hardness of the surface composite specimens was measured along the depth from the irradiated surface, and the results are shown in Figures 9(a) through (d). The measurements in all of the plots represent several sets of hardness measurements made from the surface, and the bars associated with each hardness data point represent the standard deviation of each hardness measurement at that depth. The Vickers hardness of the melted region of the T5 specimen ranges from 440 to 510 VHN (Figure 9(a)) and that of the TiC agglomerates is about 790 VHN. The hardness deviation expressed by an error bar slightly decreases as it is close to the interfacial region located at 2.5-mm depth, and the hardness abruptly drops to 175 VHN in the coarse-grained HAZ just beneath the interface. The hardness tends to gradually decrease further down in the HAZ and reaches 150 VHN in the fine-grained HAZ. The hardness of the unaltered region is about 135 VHN, and thus, the hardness of the melted region is 4 times higher than that of the unaltered original substrate. The T10 specimen also shows a hardness trend similar to that of the T5 specimen, but the maximum hardness is slightly less because of the reduced size and fraction of TiC particles (Figure 9(b)). The maximum hardness of the T20 specimen is reduced to 410 VHN, but is relatively constant as cuboidal TiC particles are evenly distributed in the structure (Figure 9(c)). The T40 specimen also shows a constant hardness in the melted region, but the hardness is lowered to 380 VHN because of the low fraction of TiC particles (Figure 9(d)). These hardness data indicate that the hardness of the melted region is 3 to 4 times greater than that of the original substrate.

IV. DISCUSSION

The microstructure of the TiC-reinforced ferrous surface composites fabricated by high-energy electron beam irradiation is composed of the melted region, the HAZ, and the unaltered original substrate region. The thickness of the melted region depends on the penetration depth of the electrons, which is determined by the electron energy and material density.[39] Since the electron energy was fixed at 1.4

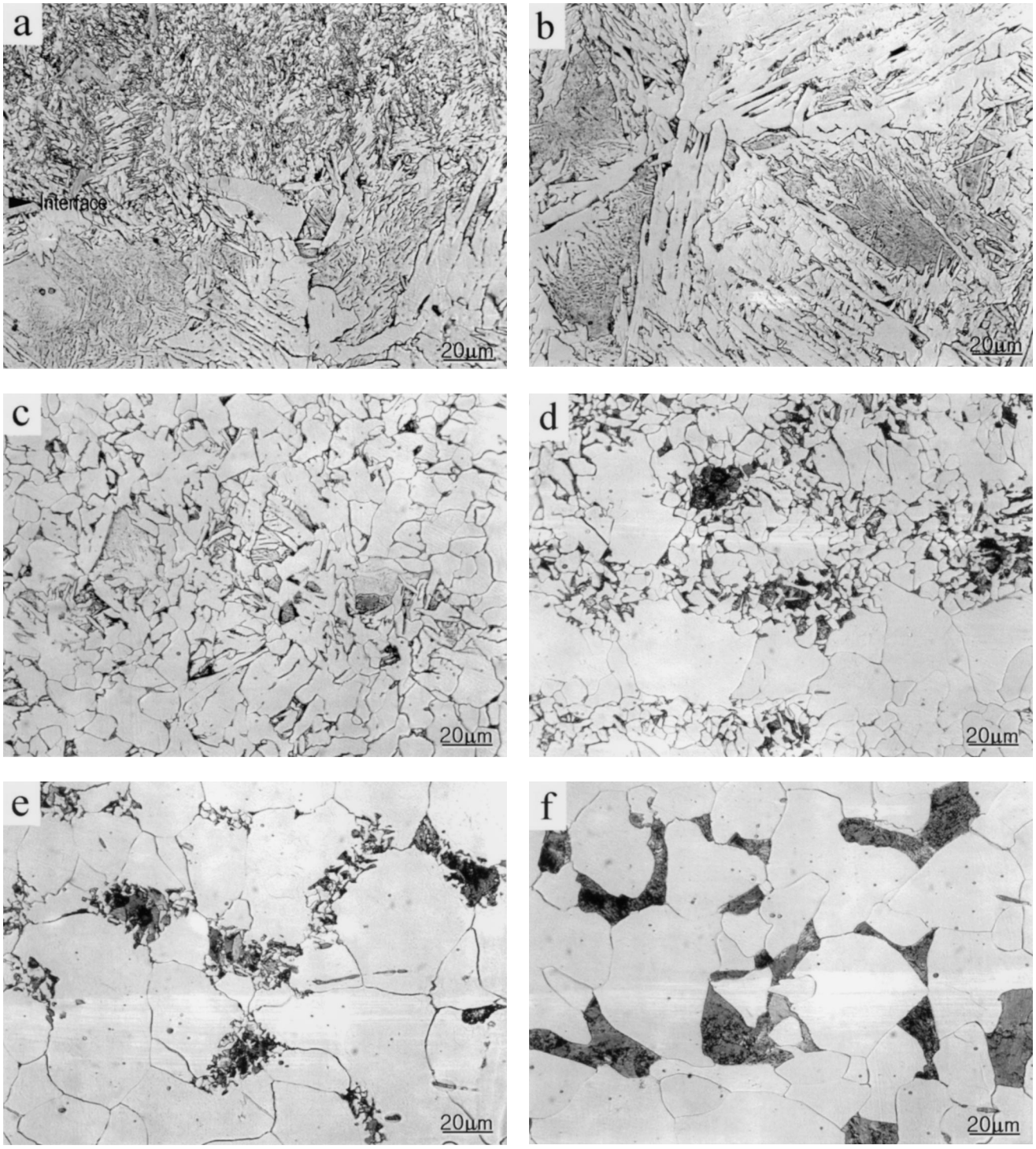

Fig. 6—Optical micrographs of the T20 specimen, showing (*a*) interfacial region, (*b*) coarse-grained HAZ, (*c*) fine-grained HAZ, (*d*) and (*e*) the region below fine-grained HAZ, and (*f*) unaltered original microstructure, which consists of ferrite and pearlite. Nital etched.

MeV and the density of the steel substrate (7.8 g/cm^3) was much higher than that of the powder mixture (1.5 g/cm^3), the irradiation depth is mostly dependent on the substrate density. Thus, the thickness of the melted region, *i.e.*, the surface composite layer, does not vary much with the flux-mixing ratio, being constant at about 2.5 mm under the present irradiation conditions.

A problem in fabricating surface composites reinforced with ceramic particles by electron beam irradiation is the inhomogeneous distribution of reinforcing phases in the melted region because the unmelted ceramic particles, or such particles that form first during solidification, have a tendency to float in the liquid pool. To overcome this problem, ceramic powders such as SiC, TiC, TiB_2, and TiN, having lower density than the substrate, are sprayed using a laser beam.[18] However, the present work achieves a homogeneous distribution of reinforcing phases by adding an appropriate amount of flux to control the fluidity of the

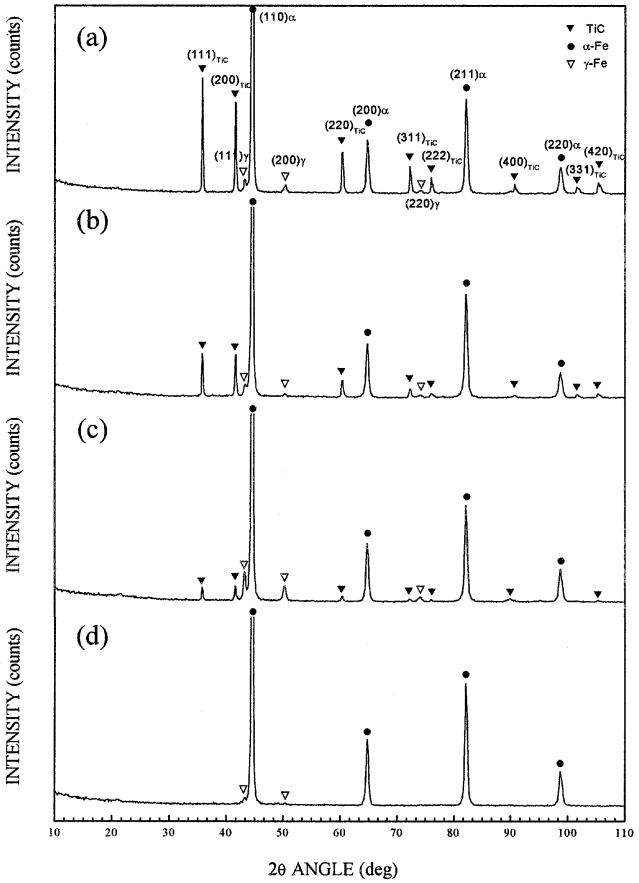

Fig. 7—X-ray diffraction data of the melted region of (*a*) the T5, (*b*) the T10, (*c*) the T20, and (*d*) the T40 specimens.

Table III. Hyperfine Parameters at 300 K

Phase	Spectrum	δ (mm/s)	Q (mm/s)	H_f (T)	References
bcc	bcc-Fe	0.00	0.00	33.0	standard
bcc + bct	Fe-M(1)	0.11	0.02	27.4	36
	Fe-M(2)	0.07	−0.04	30.7	
bct	bct-Fe(1)	0.08	0.28	26.5	30
	bct-Fe(2)	−0.05	0.20	34.3	
	bct-Fe	0.06	−0.18	33.3	
fcc	fcc-Fe	−0.05	0.00	0.0	31
Fe_3C	Fe_3C(a)	0.21	−0.06	19.7	32–36
	Fe_3C(b)	0.19	0.32	20.5	
	Fe_3C(s)	0.41	1.74	0.0	
Fe_5C_2	Fe_5C_2	0.10	0.12	23.0	35

liquid pool and to enhance the wetability between the liquid pool and ceramic powders. Generally, a flux is added to the metal melt during welding or brazing to clean the surfaces of the joint chemically, to prevent atmospheric oxidation, and to reduce impurities or float them to the surface.[23,24] Because the flux is very versatile in its components and its affect varies with the process conditions, it is very important to decide precisely what components are used and how much of them are to be mixed. The flux used in this work is a mixture of CaO and MgO (1:1 ratio in wt pct). It has been reported that the former performs a refining function in the metal melt and the latter controls the fluidity inside the liquid pool.[23,24] As the flux addition increases, the TiC agglomerates decrease in number, and the homogeneous dispersion of TiC can be achieved. This is evidence for the fact that the flux components play an important role in controlling the molten fluidity. They form slag crusts in the upper surface of the melted region after electron beam irradiation, and thus have no effect on the composition of the surface composite layer. The results of the X-ray analysis indicate that there are no phases related with the flux components (Figures 7(a) through (d)). When a small amount of flux is added, as in the T5 specimen, TiC agglomerates and pores exist in the melted region (Figures 3(a) and (b)), whereas with too much of the flux (and a lesser amount of TiC powders), the hardening effect is reduced because of the lower fraction of TiC particles inside the melted region (Figure 3(e)). According to these results, the optimum flux-mixing ratio is 10 to 20 pct.

When the steel substrate deposited with properly mixed TiC powders and flux is irradiated, the TiC powders and the substrate surface are melted, forming the melted region after the subsequent solidification. Depending on the amount of the flux addition, TiC particles in the melted region have various shapes. The T5 specimen has a lot of coarse TiC agglomerates formed in the upper part of the melted region, leading to an incomplete distribution of TiC particles. The TiC volume fraction in these agglomerated regions reaches 70 pct, and thus, it is believed that they have formed when only the surface of the powders is partially melted and solidified to a spherical shape.

The precipitation of TiC particles in the melted region and the solidification of the matrix can be explained from an Fe-Ti-C ternary phase diagram.[6,7,40] Because no flux components exist in the surface composite layer, it is possible to use this ternary phase diagram. Figure 10 shows a liquidus projection of the iron-rich region. Supposing that the matrix and TiC powders are completely melted, the liquid composition of each specimen can be plotted on the dotted line. Also, it can be assumed that the TiC agglomerates are not involved in the solidification process during irradiation because they are mainly composed of unmelted TiC powders and condensed in certain areas, as shown in Figures 3(a) and (c). The region of the TiC agglomerates is different from the dominant microstructure of the surface composite layer. Thus, the fraction of TiC agglomerates can be excluded in determining the liquid composition.

Since the TiC fractions (primary and eutectic TiC) in the T5 and T10 specimens are about the same (around 20 pct), as shown in Table II, it can be presumed that they underwent a similar solidification process. When the temperature rises to the melting point of the TiC powders and then cools down below the liquidus temperature, primary TiC particles start to nucleate and grow by diffusion of nearby Ti and C as the temperature decreases. When the temperature decreases further to the point "A," ferrite dendrites also start to form and continue growing with the TiC particles until the point "TP," the ternary quasi-peritectic temperature (1320 °C). At the point "TP," the liquid interacts with ferrite dendrites and is partially or totally transformed to austenite dendrites. This transformation continues in the solid phase, and more TiC and austenite are precipitated. Reaching the point "TE," the ternary eutectic temperature (1130 °C), austenite is finally transformed into pearlite, martensite, or bainite, depending on the cooling rate, and solidification is completed. It is

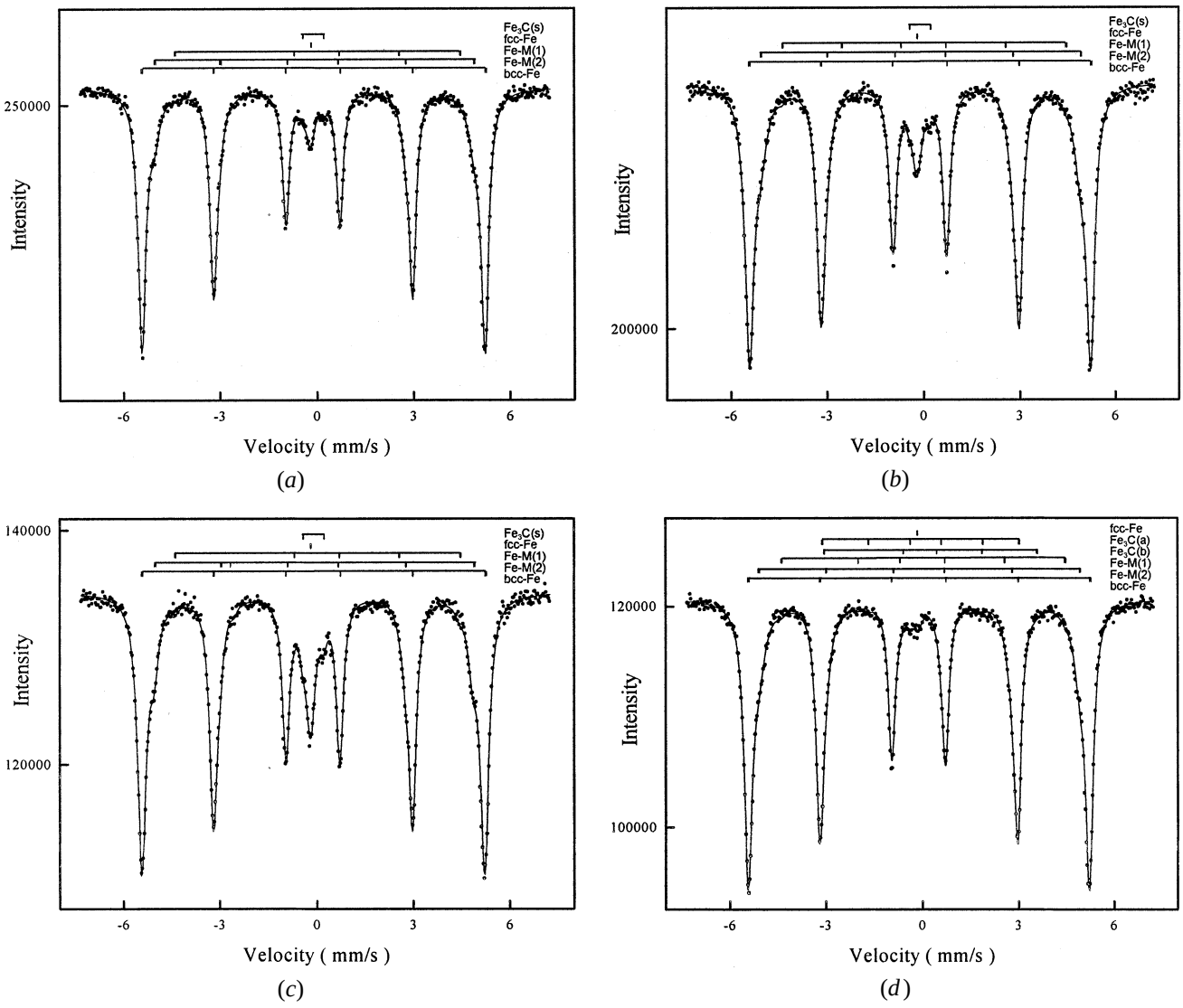

Fig. 8—Mossbauer spectra of the melted region of (*a*) the T5, (*b*) the T10, (*c*) the T20, and (*d*) the T40 specimens.

Table IV. Quantitative Analysis Data Obtained from Mossbauer Spectroscopy for the Surface Composite Specimens (Weight Percent, Error Range: ±1 pct)

Specimen	Austenite	Bainite (or Ferrite)	Fe_3C
T5	4	94	2
T10	5	93	2
T20	8	89	3
T40	2	96	2

found that the matrix of the melted region of the T5 and T10 specimens is mainly composed of bainite.

In the case of the T20 specimen, it does not have sufficient time for primary TiC to form because the temperature range from liquid to the point "A" is very narrow, unlike in the T5 and T10 specimens. Due to the lower content of Ti and C inside the liquid, TiC particles do not grow as large but form in a cuboidal shape (Figure 4(d)). In the T40 specimen, the TiC fraction in the melted region is very small, and thus, it goes through a different solidification process from the other specimens because the liquid exists within the ferrite region. Reaching the point "TP" after primary δ-Fe is precipitated, the liquid is partially or totally transformed to austenite dendrites reacting with ferrite dendrites, and TiC particles start to precipitate along the cell boundaries of the austenite dendrites. When the temperature reaches the point "TE," solidification is completed. The melted regions formed by the preceding processes are found to have microstructures that are consistent with the microstructural results of Section III–A and the phase analysis data of Section III–C.

The results of this study on the TiC-reinforced ferrous surface composites fabricated by high-energy electron-beam irradiation explain the surface composite process including the formation of the melted region and the hardness improvement. They further suggest ideas on the fabrication of surface composites with enhanced surface properties. Also, high-temperature properties of a material's surface can be improved tremendously by the formation of a considerable amount of TiC particles that are thermodynamically stable at high temperatures. Because the electron-beam irradiation can easily melt ceramic powders, the surface composites with an even distribution of thermally stable carbides on the

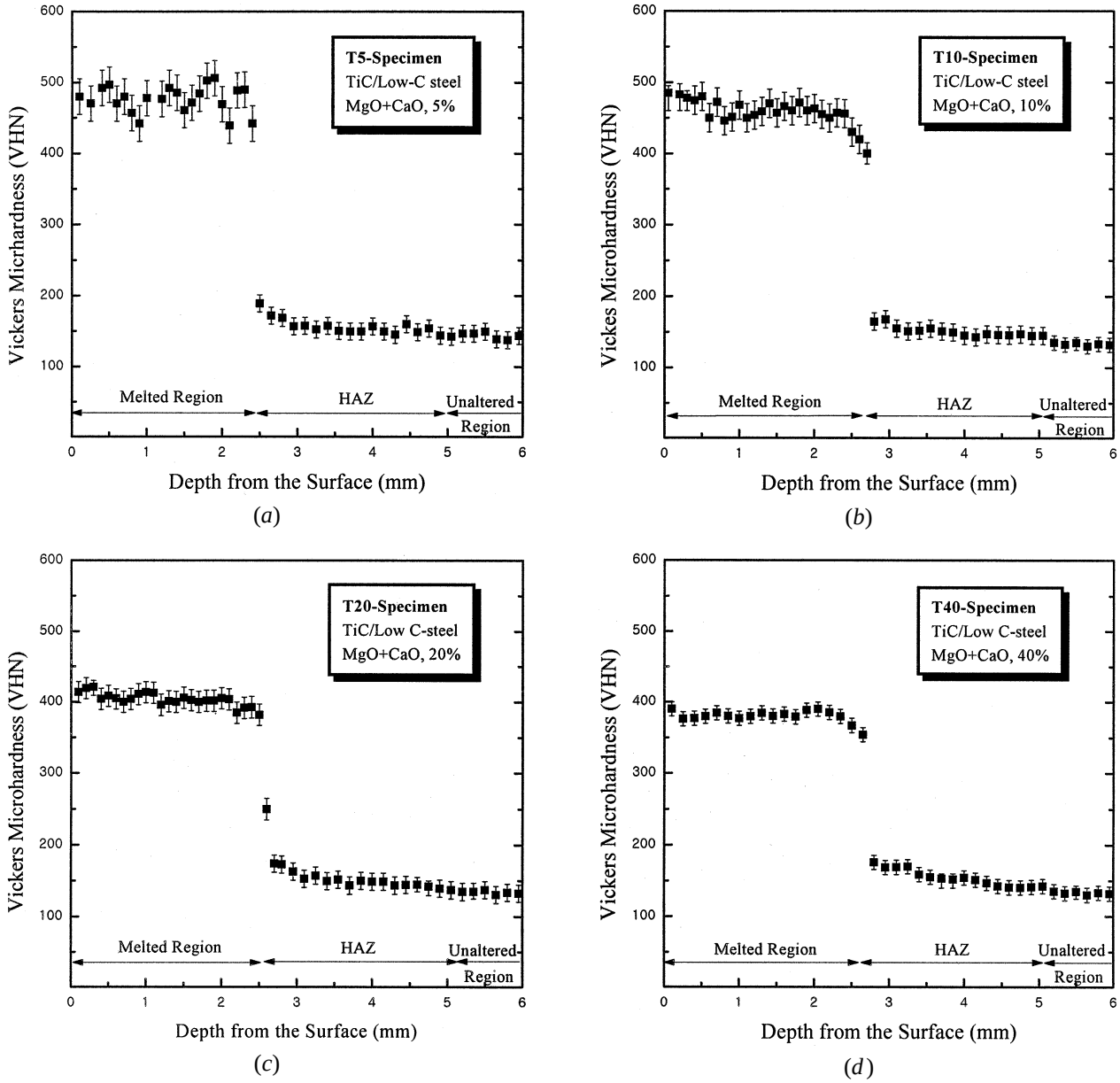

Fig. 9—Vickers hardness *vs* depth from the irradiated surface of (*a*) the T5, (*b*) the T10, (*c*) the T20, and (*d*) the T40 specimens.

substrate surface can be fabricated by *in situ* precipitation of TiC particles. Considering the energy distribution *vs* depth from the surface, the electron beam has a Gaussian distribution, whereas the laser beam shows a tendency for an exponential reduction;[41] thus, thicker surface composites can be fabricated by electron-beam irradiation. Particularly, when using a high-energy electron beam of several MeV, as in this study, the penetration depth of the electron beam further increases, thereby making it possible to form surface composites of 2 to 3 mm in thickness. As this electron-beam-irradiation method is not only economical but also leads to the development of new advanced materials with improved properties, further studies are required on selection of the ceramic powders and flux, establishment of proper mixing ratios and irradiation conditions, evaluation of high-temperature properties, and interpretation of property-enhancement mechanisms.

V. CONCLUSIONS

Surface composites reinforced with TiC particles were fabricated by high-energy electron-beam irradiation, and their microstructures and properties were analyzed.

1. Microstructures of the surface composites were composed of the melted region, HAZ, and unaltered region. The thickness of the melted regions was nearly constant at about 2.5 mm without showing much variation with the flux addition.
2. By adding the proper amount of flux, the surface composites did not have TiC agglomerates and pores and showed a homogeneous dispersion of TiC particles. When a small amount of flux was added, TiC agglomerates and pores formed, while too much flux reduced the volume fraction of TiC particles in the melted region. The optimum flux addition was found to be 10 to 20 pct.

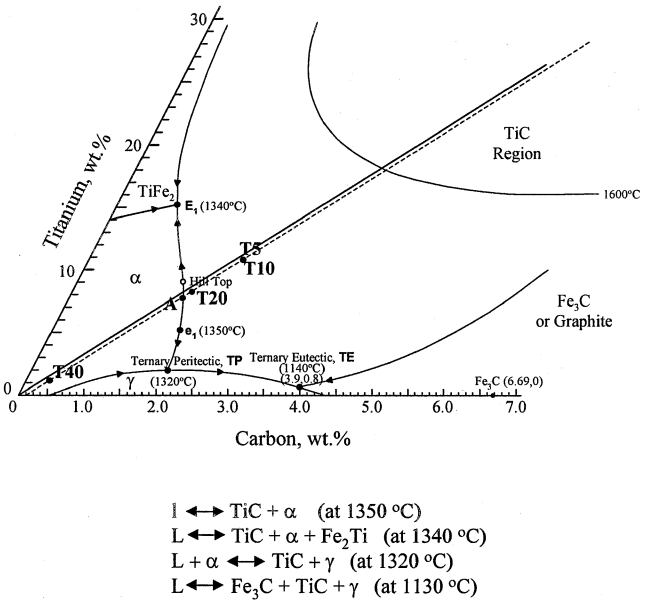

Fig. 10—Liquidus projection of the iron-rich region of a Fe-Ti-C ternary phase diagram.[6,7,40]

3. The size and shape of TiC particles in the surface composites varied with the flux addition. In the materials having less than the 10 pct flux addition, radially grown dendrites and faceted rosette-shaped particles were found, whereas in those composites having more than a 20 pct flux addition, fine cuboidal particles were mainly observed. The matrix consisted of mostly bainite, where needle-shaped eutectic TiC particles were homogeneously distributed.
4. Surface microhardness of the composite layer was 3 to 4 times higher than that of the unaltered original substrate due to the presence of TiC particles. With increasing the size and volume fraction of TiC particles, the hardness was considerably increased.

ACKNOWLEDGMENTS

The authors acknowledge the financial support of this work by the Korea Research Foundation made in the program year of 1998. The authors thank Drs. M. Golkovskii, S. Petrov, and N. Kuksanov, Budker Institute of Nuclear Physics, and Professors Yangmo Koo and Nack J. Kim, POSTECH, for their helpful discussion on the fabrication of the surface composites.

REFERENCES

1. G.C. Goetzel: *Cermets*, Reinhold, New York, NY, 1960, pp. 130-46.
2. B.K. Lograsso and R.M. German: *Progs. Powder Metall.*, 1987, vol. 43, pp. 415-39.
3. D.B. Miracle and H.A. Lipsitt: *J. Am. Ceram. Soc.*, 1983, vol. 66, pp. 592-97.
4. J.M. Panchal, T. Vela, and T. Robisch: *Advances in Powder Metallurgy and Particulate Materials—1992*, Metal Powder Industries Federation and American Powder Metallurgy Institute, Princeton, NJ, 1993, vol. 8, pp. 125-40.
5. K.-W. Chae, D.-I. Chun, D.-Y. Kim, Y.-J. Baik, and K.-Y. Eun: *J. Am. Ceram. Soc.*, 1990, vol. 73, pp. 1979-82.
6. T.Z. Kattamis and T. Suganuma: *Mater. Sci. Eng.*, 1990, vol. A128, pp. 241-52.
7. B.V. Chambers, T.Z. Kattamis, J.A. Cornie, and M.C. Flemings: *Solidification Processing*, The Institute of Metals, London, 1988, pp. 465-68.
8. B.S. Terry and O.S. Chinyamakobvu: *Mater. Sci. Technol.*, 1992, vol. 8, pp. 399-405.
9. Z. Liu and H. Fredriksson: *Metall. Mater. Trans. A*, 1996, vol. 27A, pp. 407-14.
10. Z. Liu and H. Fredriksson: *Metall. Mater. Trans. A*, 1997, vol. 28A, pp. 707-19.
11. N. Frage, L. Levin, E. Manor, R. Shneck, and J. Zabicky: *Scripta Mater.*, 1996, vol. 35, pp. 799-803.
12. K. Murakami, A. Yoshimoto, T. Okamoto, and Y. Miyamoto: *Mater. Sci. Eng.*, 1993, vol. A160, pp. 137-42.
13. N.G. Zaripov, R.R. Kabirov, and V.N. Bloshenko: *J. Mater. Sci.*, 1996, vol. 31, pp. 5227-30.
14. W. Cerri, R. Martinella, G.P. Mor, P. Bianchi, and D.D. 'Angelo: *Surf. Coat. Technol.*, 1991, vol. 49, pp. 40-45.
15. S. Ariely, M. Bamberger, H. Hugel, and P. Schaaf: *J. Mater. Sci.*, 1995, vol. 30, pp. 1849-53.
16. M. Yan, and H. Hanqi: *J. Mater. Sci.*, 1996, vol. 31, pp. 4303-06.
17. A.Y. Fasasi. M. Pons, C. Tassin, A. Galerie, G. Sainfort, and C. Polak: *J. Mater. Sci.*, 1994, vol. 29, pp. 5121-26.
18. J.D. Ayers and T.R. Tucker: *Thin Solid Films*, 1980, vol. 73, pp. 201-07.
19. A.F. Baisman, S.B. Vasserman, M.G. Golkovskii, V.D. Kedo, and R.A. Salimov: *About Surface Hardening by Concentrated Electron Beam at Atmosphere*, Budker Institute of Nuclear Physics, Novosibrsk, Russia, 1988, pp. 5-31, [preprint no. 88-73.]
20. S.-H. Choo, S. Lee, and S.-J. Kwon: *Metall. Mater. Trans. A*, 1999, vol. 30A, pp. 1211-21.
21. J.M. Poate, G. Foti, and D.C. Jacobson: *Surface Modification and Alloying by Laser, Ion, and Electron Beams*, NATO Conf. Proc. Ser. VI, Plenum Press, New York, NY, 1983, vol. 8, p. 40.
22. R.C. Weast: *Handbook of Chemistry and Physics*, 55th ed., CRC Press, Cleveland, OH, 1974, pp. D51-D52.
23. L. Davis: *An Introduction to Welding Fluxes for Mild and Low Carbon Steels*, The Welding Institute, Cambridge, United Kingdom, 1981, pp. 1-16.
24. C.E. Jackson: *WRC Bull.*, 1977, vol. 190, pp. 1-25.
25. U. Gonser: *Mossbauer Spectroscopy, Topics in Applied Physics*, Springer-Verlag, Berlin, 1975, vol. 5, p. 201.
26. S.-J. Kwon, S.J. Oh, J.H. Kim, S.H. Kim, and S. Lee: *Scripta Mater.*, 1999, vol. 40, pp. 131-37.
27. J.Y. Koo and A. Ozekcin: in *Welding Metallurgy of Structural Steels*, J.Y. Kim, ed., TMS, Denver, CO, 1987, pp. 119-35.
28. K. Uchino and Y. Ohno: *Proc. 7th Int. Conf. on Offshore Mechanics and Arctic Engineering*, Houston, TX, ASME, Golden, CO, 1988, pp. 159-65.
29. R.W.K. Honeycombe: *Steels, Microstructure and Properties*, Edward Arnold, London, 1981, pp. 31-33.
30. J.-M.R. Genin: *Metall. Trans. A*, 1987, vol. 18A, pp. 1371-88.
31. E.D. Cabanillas, L. Terminiello, N.A. Cantalejos, R. Versaci, and R.C. Mercader: *Mater. Sci. Eng.*, 1992, vol. A150, pp. 113-16.
32. M. Ron and Z. Mathalone: *Phys. Rev. B*, 1971, vol. 4, pp. 774-77.
33. F. Aubertin, L. Abada, and U. Gonser: *Hyperfine Interactions*, 1998, vol. 111, pp. 201-04.
34. M. Ron and H. Shechter: *J. Appl. Phys.*, 1968, vol. 39, pp. 265-75.
35. H. Bernas, I.A. Campell, and R. Fruchart: *J. Phys. Chem. Solids*, 1967, vol. 28, pp. 17-24.
36. S.J. Choi, S.-J. Kwon, S.-H. Choo, and S. Lee: *Mater. Sci. Eng.*, 1999, vol. A265, pp. 208-16.
37. U. Gonser: *Mossbauer Spectroscopy, Topics in Applied Physics*, Springer-Verlag, Berlin, 1975, vol. 5, p. 15.
38. C. Kittel: *Introduction to Solid State Physics*, 6th ed., John Wiley and Sons, Inc., New York, NY, 1986, p. 110.
39. S. Schillerk, U. Heisig, and S. Panzer: *Electron Beam Technology*, John Wiley & Sons, Ltd., New York, NY, 1982, ch. 1.
40. Y. Murakami, H. Kimura, and Y. Nishimura: *Trans. Nat. Res. Inst. Met.*, 1959, vol. 1, pp. 7-21.
41. J.A. Knapp and D.M. Follstaedt: in *Laser and Electron Beam Interactions with Solids*, B.R. Appleton and G.K. Celler, eds., North-Holland, New York, NY, 1982, p. 407.